Journal of Vacuum Science Technology B

Mixed Mathematical and Experimental Modeling of Electrospun Metal Oxide Supercapacitor Electrodes

Running title: Mixed Modeling of Electrospun Electrodes

Running Authors: Brockway et al.

Molly C. Brockway, [1,a)] Dennis J. Moritz,[2] John J. Borkowski,[2] and Jack L. Skinner[1]

[1]Montana Technological University, Mechanical Engineering, 1300 W Park St, Butte, MT 59701
[a)]Montana University System, Materials Science PhD, MT USA
[2]Montana State University, Mathematical Sciences, Bozeman, MT 59717

[a)] Electronic mail: mbrockway@mtech.edu

Supercapacitors are an important energy storage technology that combine the high energy density of batteries with the high power density of capacitors. Freestanding Mn_2O_3 electrodes fabricated via electrospinning and calcination have the potential to provide high power and energy densities with low fabrication costs. In this work, a theoretical model is produced to describe the effects of the electrospun structure on electrode performance. The model uses theoretical predictions of capacitive and faradaic energy storage, based on system parameters measured from real electrodes to produce a realistic model that can be used for engineering design and optimization of the electrodes. Porosity-controlled discharge time and extremely stable energy densities are predicted by the model. Results are compared to discharge curves of a real electrode to examine model fidelity.

I. INTRODUCTION

Supercapacitors are an important developing technology for applications such as renewable energy storage, load leveling for power grids, and portable electronics.[1–3] Although already available for a range of commercial uses including hybrid and electric vehicles,[4] public transportation,[5] and consumer electronics[6] performance must be improved to meet the demands of future systems by developing new materials and improving structures and interfaces. Compared to batteries, supercapacitors have charge and discharge rates on the order of seconds or minutes, giving them uniquely high power densities; compared to electrolytic capacitors, the total energy density is several orders of magnitude higher.[7,8] The combination of high energy and power densities makes supercapacitors uniquely well suited to complement or replace batteries in many energy storage applications.

While carbon-based supercapacitors are currently most common, transition metal oxides are promising for their potential pseudocapacitive abilities, wherein fast and highly reversible faradaic reactions complement the double layer capacitance of the active material to increase specific capacitance by potentially orders of magnitude.[9,10] Supercapacitors are composed of two high surface area electrodes separated by an ionically conducting electrolyte and separator. Upon application of a potential to the two electrodes, ions are reversibly adsorbed onto the electrode surface due to polarization at the electrode-electrolyte interface. Pseudocapacitors additionally participate in electron exchange between ions and the active materials at the surface, without the ion intercalation present in Li-ion batteries.[11] A lack of dimensional changes in the structures leads to exceptional cycling stability, with thousands of cycles possible with minimal loss in energy storage capacity.[12] Of the metal oxides, manganese oxides are attractive owing

to their low cost, low toxicity, and high performance.[13] Although RuO_2 is the highest-performing metal oxide, with a theoretical capacitance of over 2000 F/g, it is highly toxic and extremely expensive. MnO_2, on the other hand, has theoretical capacitances of around 1300 F/g, while being available at a fraction of the cost and without the health risks of RuO_2. Mn_2O_3 is another manganese oxide with a somewhat lower capacitive performance of around 600 F/g,[14] but is easily prepared via direct calcination of precursors in air and is therefore attractive for experimental purposes and testing novel electrode morphologies.

Because the mechanism of charge storage is purely a surface interaction, high active surface area in the electrodes is essential to improving supercapacitor performance. Nanostructures possess extraordinarily high specific surface areas and have thusly been at the forefront of supercapacitor research.[3,9] Processing metal oxide nanostructures into usable supercapacitor electrodes traditionally involves mixing the active nanomaterials with binders and conductive agents before pasting onto charge collectors and subsequent drying. Conductive agents such as carbon black take up a large volume of the final electrodes and may limit electrolyte access to the nanomaterials, resulting in a higher fraction of dead space and underutilization of the ultrahigh surface areas of the active nanomaterials. Additionally, achieving high energy and power densities simultaneously has been a difficulty, with high power density frequently coming at the expense of energy density.[15]

One method for producing high surface-area nanofiber-based electrodes is electrospinning and thermal processing. Electrospinning is a facile and versatile fabrication technique, and can be used to produce carbonaceous or inorganic nanofibers

with tunable structures.[16] Most frequently, electrospun materials are processed into electrodes using the traditional methods previously described, but to fully take advantage of the facile nature of electrospinning, it is important to minimize the necessary processing for electrode fabrication. Recently, the nonwoven web structure of electrospun materials has been under investigation to produce electrodes from carbon nanofibers,[17,18] metal oxides,[19] and oxide-carbon composites.[20] Freestanding electrodes produced by electrospinning naturally possess high specific surface area and electrolyte permeability and may be tuned to exhibit a variety of compositions.

Previously, we have reported a manganese oxide-based freestanding web electrode structure that eliminates binders and conductive agents.[21] In the freestanding structures, polymer nanofibers containing oxide precursors are electrospun directly onto charge collectors and calcined to yield pure oxide nanofibers. The performance of the freestanding electrodes is controlled largely by the morphologies of the electrospun fiber webs, including fiber diameter and porosity of the structure, which cannot be independently modified due to the limitations of the fabrication procedure. Toward the goal of optimization, a model of electrode performance based on actual system parameters as well as theoretical processes will allow research to focus on the areas of greatest importance. A more complete understanding of the effects of structure morphology will inform future efforts towards structure optimization by revealing the effects of various parameters on electrode performance.

Modeling of nanostructured and porous metal oxide supercapacitors has been extensively performed, as accurate simulations of the structures and processes are essential to understanding and improving performance. In 1975, Tiedemann and Newman

presented an early model for the double-layer charging behavior of porous lead oxide electrodes.[22] Later, Srinivasan and Wiedner examined the effects of cell design and operation parameters including electrode thickness, electrode and electrolyte resistances, temperature, and current density on power and energy densities of porous electrodes.[23] To introduce faradaic reactions into capacitive systems, Pillay and Newman modeled the effects of side reactions on charging and cycling of porous electrodes.[24]

Lin's first model combining pseudocapacitive and double layer processes in a porous metal oxide supercapacitor structure has provided the basis for many further models of metal oxide supercapacitor systems.[25] The Lin model has been expanded on by application to oxide/carbon composite systems with proton diffusion effects;[26,27] describing the behavior of asymmetrical supercapacitors;[28–30] describing hybrid battery/supercapacitor systems;[31–33] use with other metal oxides;[34–36] examining varying geometries including nanorods,[37] interdigitated electrodes,[38] and changes in electrode thickness and porosity;[39] and to account for self-discharge and side reactions.[40,41] Other models integrate more complex descriptions of double-layer capacitance to more accurately account for ion interactions in the electrolyte and with the electrode surface[42] or describe moving reaction fronts through the electrode thickness.[43] Conversely, some research has also focused on providing simplified models for easier implementation.[44]

A common aspect of analytical models developed to describe supercapacitor behavior is lack of integration with experimental results. Many models are verified by comparison to other theoretical results and use only assumed values that may not describe the system realistically. Several models have been compared to or verified against experimental results[35,39,45] or use values derived from experimental results,[46,47] but a lack

of widespread integration exists between theoretical and experimental models for describing metal oxide-based supercapacitor behavior. In this work, we combine experimentally derived system values with theoretical processes and reactions to describe the unique freestanding web supercapacitor electrodes as a realistic system. The model is developed from and for Mn_2O_3 webs but may be expanded to other metal oxide systems fabricated with similar methods.

II. EXPERIMENTAL

A. Electrode Fabrication

Electrodes were fabricated via electrospinning and subsequent calcination. Fibers were electrospun from a solution consisting of 20 *wt*% polyvinylpyrrolidone (PVP, MW = 1,300,000, Sigma-Aldrich) and 8 *wt*% manganese (II) acetate ($Mn(ac)_2$) in a solvent of 1:1 deionized water : ethanol (≥99.5 %, Sigma-Aldrich) by mass. Manganese acetate was added to the solution as $Mn(ac)_2 \cdot 4H_2O$ (≥99 %, Sigma-Aldrich), and the mass of water contributed by the acetate tetrahydrate was factored into the mass of water added into the solvent. The solution was mixed until homogeneous (~4 h) and used immediately. Fibers were electrospun in a Spraybase vertical electrospinner equipped with a 22-gauge needle at high voltage, set at a 4.5 cm spacing from the grounded collection plate. Solution was delivered through the needle at 0.40 mL/h, and voltage was held at 6.0 kV. Electrospun mats were deposited for 10 min at a time before removal to storage in a dessicator to prevent moisture degradation.

Electrospun fiber mats were calcined in a 2-in-diameter tube furnace (MTI Corp, USA) in air. The furnace was ramped at 10 °C/min to 600 °C, then held at temperature

for 6 h before cooling to room temperature. Once cooled, 15-mm diameter electrodes were cut from the mats and assembled into full cells for electrochemical characterization. Phase produced by these fabrication conditions has previously been characterized with XRD to confirm the sole presence of Mn_2O_3.[21]

B. Imaging and Visual Measurements

Scanning electron microscopy (SEM) was used to measure fiber mat thickness, porosity, and average fiber diameter. Samples were cut from the calcined fiber mats and lightly gold coated before imaging with a Tescan Mira3 FE-SEM at 15 kV. From each fiber mat, planar and cross-sectional images were collected at multiple locations. Image analysis to determine fiber thickness, mat thickness, and porosity was performed in ImageJ. For fiber thickness, the average of 20 diameter measurements from five locations was taken as average diameter. Fiber mat thickness was taken as the average of 20 measurements from cross-sectional images.

Porosity was measured from SEM micrographs by threshholding the image so that all fibers were displayed as white pixels, and voids were black (Fig. 1).

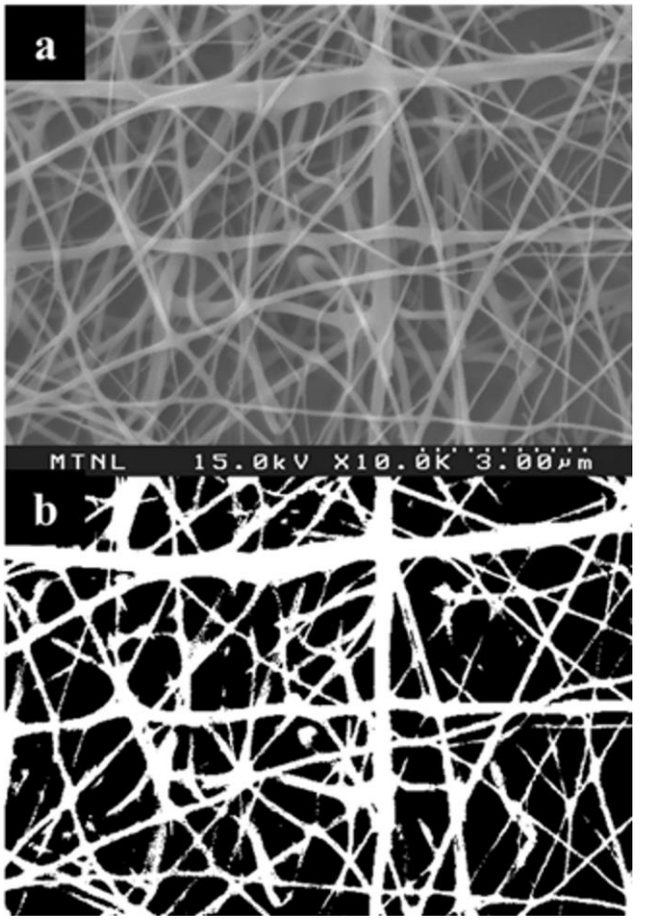

Figure 1: SEM micrographs of electrospun fiber mat electrodes (a) used to measure porosity by threshholding (b) and calculating ratio of black pixels to total pixels.

The ratio of black pixels to total pixels in the image then represented fiber mat porosity. Porosity was measured from 10 locations and averaged to yield the fiber mat porosity used in the model.

C. Electrochemical Characterization

Electrodes were tested as symmetrical cells in a two-electrode split cell (MTI Corp., USA) with 15 mm electrodes cut from the calcined fiber mats, a glass microfiber filter separator (Whatman, Grade GF/F), and 1.0 M Na_2SO_4 (≥99.0 %, Sigma-Aldrich) electrolyte. A two-electrode configuration was used to characterize the cells with linear

sweep voltammetry (LSV), electrochemical impedance spectroscopy (EIS), and galvanostatic charge-discharge (GCD), with a Gamry 1010E electrochemical test station used to conduct all tests. Each test was performed on three cells, and the calculated values were taken as the average of the measurements.

Transfer coefficients and exchange current were calculated from Tafel plots generated from LSV. Linear sweeps were taken from -0.1 V to 0.1 V at 0.5 mV/s, and the results were plotted as log(*current*) vs potential. Linear approximations were fit to the linear regions of the curve, and the anodic and cathodic transfer coefficients were calculated according to

$$\alpha_a = \frac{RT}{nF}\frac{\partial \ln i_a}{\partial E} \qquad (1)$$

$$\alpha_a + \alpha_c = 1 \qquad (2)$$

where R is the ideal gas constant, T is absolute temperature, n is the number of electrons involved in the reaction, F is the Faraday constant, and the derivative term is the slope of the linear region of the Tafel plot.

Electrochemical impedance spectroscopy was conducted on the cells from 1 MHz to 0.1 Hz, with 0 V DC and 5 mV AC applied. Bode and Nyquist plots generated from EIS were fit with equivalent circuit models to describe the observed behavior and isolate double layer capacitance from pseudocapacitive energy storage modes. The same equivalent circuit model was used to describe all samples.

D. Model Implementation

The theoretical model was implemented in R,[48] with the package deSolve[49] used to solve the system of ordinary differential equations. For each iteration, the spatial domain was divided into 50 boxes, and the time domain was given a step size of 0.1 s.

For generating Ragone plots at current densities above 100 A/g, the time domain was given a step size of 0.01 s.

III. MODELLING

Lin's model of a porous metal oxide-based supercapacitor was used as the foundation for the model presented herein.[25] In Lin's model, two $RuO_2 \cdot xH_2O$ nanoparticle-based electrodes are separated by an ionically conducting separator and H_2SO_4 electrolyte. To adapt the model to the Mn_2O_3 fibrous web-based system described by our work, new equations were derived to describe the faradaic reactions occurring in the electrodes and the geometric relationships between fiber size, porosity, and specific surface area. Fibers are approximated as non-porous cylinders; temperature, electrolyte concentration, and DL capacitance are assumed to be invariant with potential; and side reactions, leakage, and self-discharge are ignored.

Double layer capacitance was extracted from faradaic energy storage by fitting an equivalent circuit model to EIS scans conducted at high frequencies (Fig. 2).

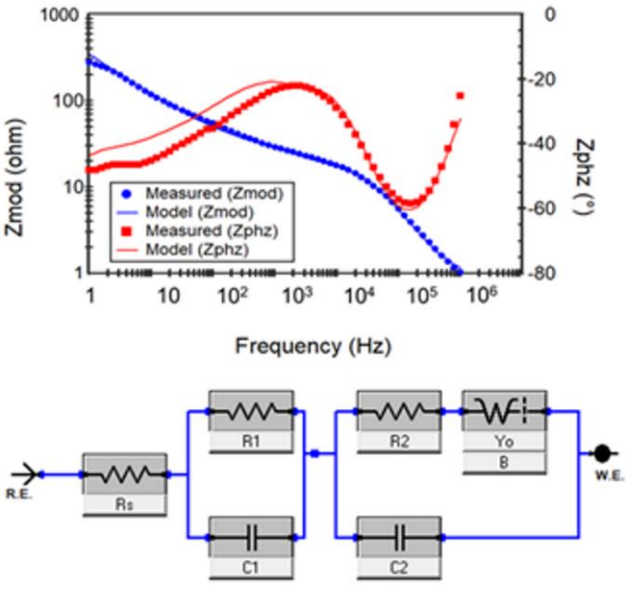

Figure 2: A typical Bode plot for electrospun Mn_2O_3 electrodes, with the equivalent circuit model overlaid onto data. A representation of the equivalent circuit model used to measure system parameters is also displayed. Color available online.

In the equivalent circuit model, R_s represents electrolyte resistance, RC component 1 is DL capacitance, and RC component 2 represents the faradaic energy storage. The Warburg component, with parameters Y_o and B, describes the limitations introduced by ion diffusion in the system. The model fits well in the high-frequency range, where DL capacitance (C_d) is observed, and departs from the data in the low-frequency range, where kinetically slow effects such as diffusion and chemical reactions become more dominant. Because only C_d and electrolyte resistance were extracted from EIS scans, the poorer fit in the phase shift data at low frequency was not considered significant to the values. The electrolyte resistance and DL capacitance were then taken as R_s and C_1, respectively, as calculated for the equivalent circuit model. The faradaic reactions occurring between the Mn_2O_3 electrodes and the Na_2SO_4 electrolyte during charge and discharge are expressed as

$$[Mn^{3+}]_2O_3 + SO_4^{2-} \overset{charge}{\rightleftharpoons} [Mn^{4+}]_\delta [Mn^{3+}]_{2-\delta}O_3 \cdot 0.5\delta[SO_4^{2-}]_{ads} + \delta e^- \quad (3)$$

for the positive electrode, and

$$[Mn^{3+}]_2O_3 + Na^+ + \delta e^- \overset{charge}{\rightleftharpoons} [Mn^{2+}]_\delta [Mn^{3+}]_{2-\delta}O_3 \cdot \delta Na^+_{ads} \quad (4)$$

for the negative electrode, where δ is the state of charge of the electrode. During charging, the reduction of Mn^{3+} to Mn^{2+} in the negative electrode is compensated by sodium ion adsorption from the electrolyte, and oxidation to Mn^{4+} is countered by sulfate ion adsorption.[50]

The faradaic transfer current in the system, j_f, is described by the Butler-Volmer equation

$$j_f = i_0\{exp[\alpha_a f(E - U_a)] - exp[\alpha_c f(E - U_c)]\} \quad (5)$$

where i_0 is the exchange current density of the Faradaic reaction; f is equal to F/(RT), with F being Faraday's constant, R the ideal gas constant, and T absolute temperature; α_a and α_c are the anodic and cathodic transfer coefficients for the reactions, and U_a and U_c are the equilibrium potentials at the anode and cathode, respectively. U is a function of the state of charge, which is represented by θ as the fraction of oxidized species in the electrode. To obtain the relationship between state of charge and equilibrium potentials, the charge and discharge curves obtained from LSV are integrated to yield total electrode charge, Q. State of charge (SOC) is then calculated according to

$$\delta = \frac{Q}{2mF} \qquad (6)$$

where m is moles of Mn_2O_3 present in the electrode, based on mass. SOC is then plotted against potential between 1 V and 0 V (Fig. 3).

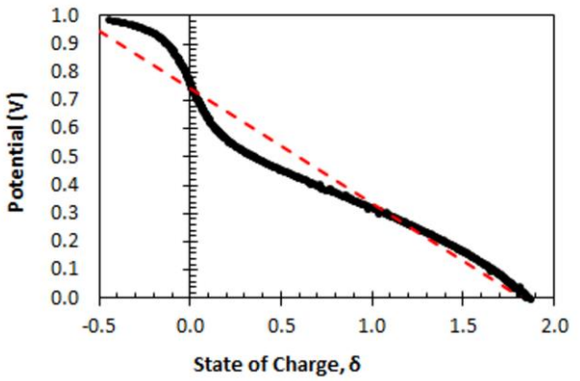

Figure 3: Voltage of Mn_2O_3 electrospun electrodes as a function of state of charge obtained by integrating the LSV curve, with the linear approximation displayed as a dotted line. Color available online.

To approximate the relationship between state of charge and potential, a linear approximation was fit to the curve over the entire range. The inflection point around $\delta = 0$ and negative SOC region are due to redox activity in the Mn_2O_3 electrodes and indicate that pseudocapacitive mechanisms are necessary in the material for reaching the 1 V

charge. The linear approximation has an R^2 value of 0.952, which is considered adequate for the purpose of estimating state of charge over the voltage range. U_a and U_c are related to fraction of oxidized species by

$$U_a = 0.371\theta \quad (7)$$

$$U_c = 0.371(\theta - 0.406) \quad (8)$$

which is estimated from the relationship between potential and state of charge for an Mn_2O_3 electrode (Fig. 3), according to the equation for the linear approximation.[25,51] Faradaic charge of the electrode relates θ and j_f by

$$\theta = \frac{Q_f - Q_{f,red}}{Q_{f,ox} - Q_{f,red}} \quad (9)$$

$$\frac{\partial Q_f}{\partial t} = s_v j_f \quad (10)$$

where Q_f is the faradaic charge of the electrode, $Q_{f,red}$ is charge of a fully reduced electrode, $Q_{f,ox}$ is charge of a fully oxidized electrode, and s_v is the active surface area per unit volume of the electrode. The charges of fully reduced and oxidized equations are assumed constant and are calculated according to

$$Q_{f,ox} = \frac{s_v \delta F}{h^2 L_A} \quad (11)$$

$$Q_{f,red} = 0 \quad (12)$$

where h is the lattice length on the surface of the electrode, and L_A is Avogadro's number. State of charge, δ, for a fully charged electrode is taken as 2 according to Eq. (3) and (4). Equations (5), (9), and (10) are combined into one of the main governing equations of the model as

$$\frac{\partial \theta}{\partial t} = \frac{s_v j_f}{Q_{f,ox} - Q_{f,red}}. \qquad (13)$$

The second governing equation describes changes in electrode potential through the thickness of the electrode by

$$\frac{\partial^2 E}{\partial \xi^2} = \tau \frac{\partial E}{\partial t} + \frac{\tau}{C_d} j_f \qquad (14)$$

where ξ is the dimensionless distance describing spatial location within the electrode; C_d is the double layer capacitance per unit surface area of the electrode, obtained by dividing DL capacitance obtained from EIS curve fitting by the total surface area contained within the electrode; and τ is the double layer time constant of the system. The time constant is further defined by

$$\tau = s_v C_d L^2 \left(\frac{1}{\sigma} + \frac{1}{\kappa_p}\right) \qquad (15)$$

where L is the total thickness of one electrode, σ is the bulk conductivity of the electrode matrix, and κ_p is the conductivity of the electrolyte within the pores of the electrode, expressed as

$$\kappa_p = \kappa_0 \epsilon^{1.5} \qquad (16)$$

where κ_0 is bulk conductivity of the electrolyte and ϵ is the electrode porosity. The thickness of the electrode was allowed to vary with changing fiber diameter as

$$L = \frac{L_{obs} D}{D_{obs}} \qquad (17)$$

where L_{obs} and D_{obs} are the observed electrode thickness and average fiber diameter, as measured from SEM micrographs. The thickness variation operates under the assumption

that a constant number of fiber layers are deposited with changing diameter. The relationship between electrode surface area and porosity is described by

$$s_v = \frac{4(1-\epsilon)}{D} \quad (18)$$

$$\epsilon = 1 - \left(\frac{\pi D^2 l}{4}\right) \quad (19)$$

where D is fiber diameter and l is the length of fiber deposited in the unit cell during electrospinning. Because the freestanding electrospun morphology prevents any packing of the structures as would be expected with free-flowing nanoparticles, it was necessary to expand the porosity observed in the fabricated electrospun webs to similarly fabricated structures composed of fibers with different diameters. To do so, a constant length of deposited fiber within the unit cell was assumed, which fixes the fibers in space and allows diameters to increase or decrease without affecting the center-to-center fiber spacing. A length value is obtained by solving Eq. (19) for l using the observed porosity and average fiber diameter, which can then be carried forward to calculate ϵ and s_v for any fiber size. Additionally, the diameter that results in zero porosity is calculated and used as the upper limit of D in the model. The unique effect of the fixed-fiber model is that as D increases, specific surface area for a unit cell of the electrode also increases. Without packing, increasing fiber diameter consumes void space in the electrode and allows for more effective space utilization; however, it is important to note that surface area per fiber volume still decreases with increasing diameter, as is expected from scaling effects.

The boundary and initial conditions were set according to the assumption that at the interface between electrode and current collector ($\xi = 0$), all current arises from the

current collector, and at the electrode surface farthest from the current collector ($\xi = 1$), current arises exclusively from the electrolyte phase. At the $\xi = 0$ interface,

$$\frac{\partial E}{\partial \xi} = -\frac{i_{cell} L}{\sigma} \qquad (20)$$

where i_{cell} is the applied or requested cell current density. At the $\xi = 1$ interface, the potential flux boundary is

$$\frac{\partial E}{\partial \xi} = -\frac{i_{cell} L}{\kappa_p}. \qquad (21)$$

Additionally, it is assumed that the fraction of oxidized species within the electrode, θ, will be constant across the thickness of the electrode, giving the boundary condition

$$\frac{\partial \theta}{\partial \xi} = 0. \qquad (22)$$

The initial conditions are set for discharge such that at time $t = 0$, $E = 1$ V, and $\theta = 1$. A complete list of model parameters and their values is presented in Table 1.

Table I: List of model parameters used to describe discharge of freestanding electrospun electrodes. The model parameters include the measured values for the parameters that are manipulated during discharge modeling.

Parameter	Value	Source
Exchange current density, i_0	1.29×10^{-5} A	Measured (LSV)
Anodic transfer coefficient, α_a	0.664	Measured (LSV)
Cathodic transfer coefficient, α_c	0.336	Measured (LSV)
Equilibrium potential at anode, U_a	0.371θ V	Eq. (7)
Equilibrium potential at cathode, U_c	$0.371(\theta - 0.406)$ V	Eq (8)
Charge of a fully oxidized electrode, $Q_{f,ox}$	0.391 C at D = 112 nm	Eq. (10)
Charge of a fully reduced electrode, $Q_{f,red}$	0 C	Lin, et. al [25]
Specific surface area of electrode, s_v	2.22×10^5 cm^2/cm^3 at D = 112 nm	Eq. (17)
Lattice spacing at electrode surface, h	9.41×10^{-8} cm	Geller [52]
System time constant, τ	1.05×10^{-3} at D = 112 nm	Eq. (14)
Areal capacitance of electrode, C_d	1.51×10^{-6} F/cm^2	Measured (EIS)
Electrode thickness, L	4.08×10^{-5} cm at D = 112 nm	Measured (SEM)
Conductivity of electrode matrix, σ	1×10^{-5} S/cm	Hong, et. al [53]
Conductivity of bulk electrolyte, κ_0	0.0667 S/cm	Measured (EIS)
Electrolyte conductivity within pores, κ_p	0.051 S/cm at D = 112 nm	Eq. (15)

Fiber diameter, D	Between 100 and 250 nm	Assumed
Electrode porosity, ϵ	0.8371 at D = 112 nm	Measured (SEM)

With D and i_{cell} as the manipulated variables, and all other model parameters measured or assumed, Eq. (13) and (14) are a system with two equations and two unknowns, E and θ. Diameters were set between 100 nm and 250 nm to stay below the upper fiber diameter limit of 276 nm, where the structure achieves zero porosity. Current densities between 1 A/g and 5000 A/g were used to examine the effects of increasing power density on energy density of the structures. Local electrode potential and fraction of oxidized species were solved over defined time ranges at locations throughout the depth of the electrode.

IV. RESULTS AND DISCUSSION

The electrospun electrodes were imaged with SEM and TEM to examine the structure and morphology of the oxide fibers (Fig. 4).

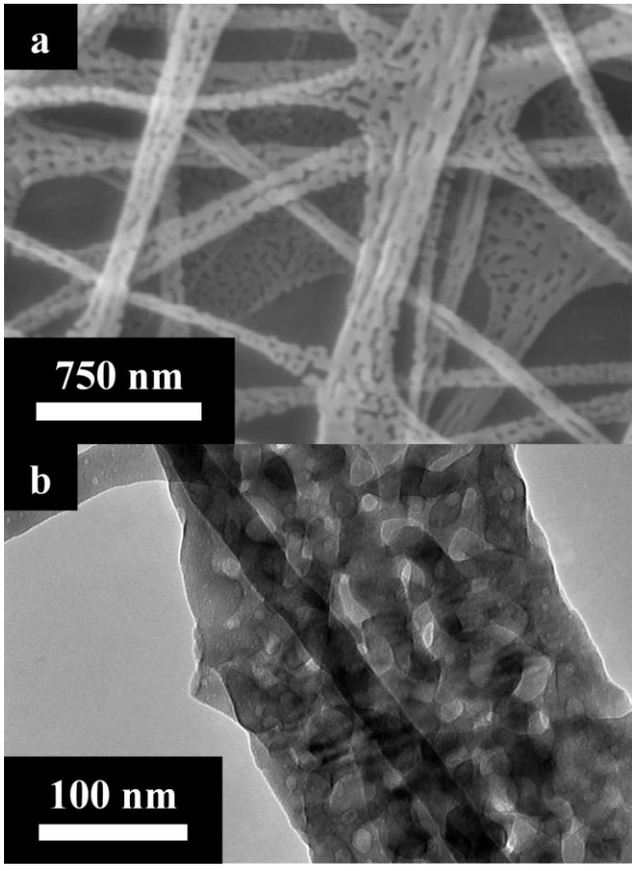

Figure 4: Micrograph images of electrospun Mn_2O_3 fibers. (a) SEM showing fiber porosity and layered structure. (b) TEM showing interior porosity of electrospun oxide fibers.

After calcination, the electrospun fibers demonstrate a highly porous structure. The porosity results from the mechanism of fiber formation during heat treatment. Manganese acetate in the composite electrospun fibers converts to oxide between 260 and 310 °C. During the conversion, regions of $Mn(ac)_2$ in the fibers form an interconnected manganese oxide network that preserves the fiber morphology upon polymer burnout, which occurs between 400 and 450 °C.[54] Further calcination at 600 °C allows full conversion to Mn_2O_3 and densification of the structures. Both SEM and TEM examination reveal a high degree of porosity in the fibers, which is highly desirable for supercapacitor applications due to the additional surface area that the porosity provides.

The primary variable manipulated for the mathematical and experimental model was fiber diameter, *D*. Discharge curves were simulated between 1 V and 0 V for electrospun fiber mats with changing fiber diameter (Fig. 5). Charging curves were assumed to simply be the reflection of the discharge curves.[25]

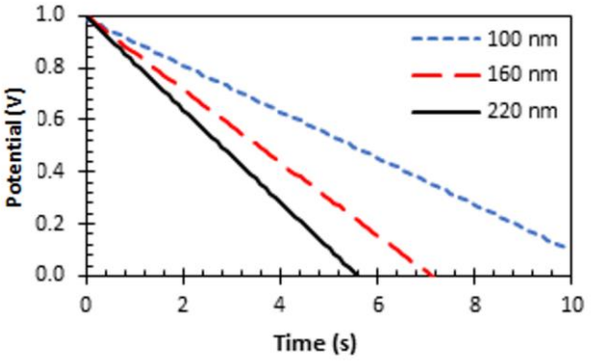

Figure 5: Discharge curves generated from the mathematical model for freestanding web electrodes with fiber diameters of 100, 160, and 220 nm at a current density of 1 A/g. Color available online.

The electrodes exhibit linear discharge to 0 V, with discharge time increasing for decreasing fiber diameter. The linear nature of the discharge curves results from the model combining capacitive and Faradaic response from t = 0, assuming no change in capacitance or reactivity over time or kinetic delay of the initial faradaic response. As fiber diameter increases, discharge time shortens due to decreased specific surface area relative to active volume. Although fixing the fibers in space causes increased specific surface area of the electrode with increasing fiber diameter, the effect results from consumption of void space between the fibers. The mass-based scaling effect of surface area to volume ratios decreasing with increasing linear dimensions still describes the active volume of the fibers themselves, so as current density is scaled to mass, it is controlled by fiber volume minus void space, rather than the total electrode volume.

Because a constant current density was used to simulate real application conditions, the total cell current applied to the electrodes scales with $1/D^2$ (for cylindrical fibers), while the active surface area scales with 1/D. Applied current therefore increases more rapidly than energy storage sites and total capacity, so the discharge time must decrease with increasing fiber diameter.

However, the effect of fiber size on discharge time is not solely determined by scaling effects, with a slowed response observed for electrodes with fiber diameters above 230 nm (Fig. 6).

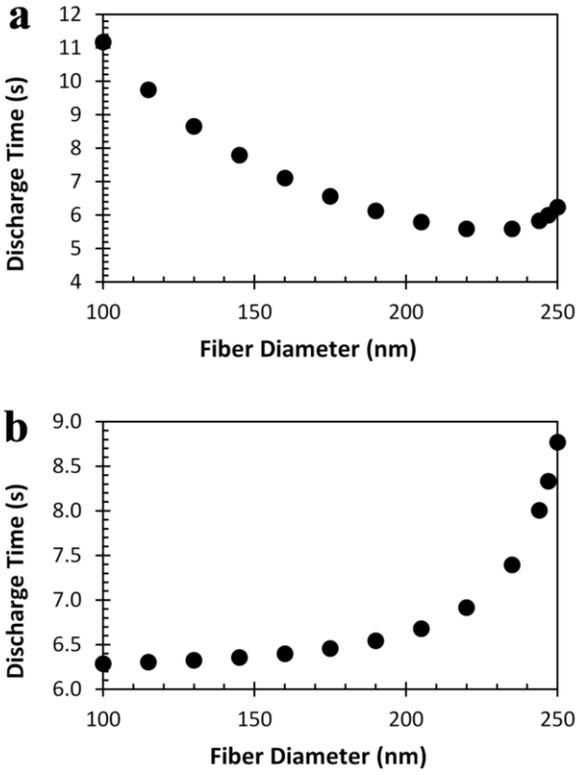

Figure 6: (a) Time to fully discharge for electrodes with varying diameter, discharged from 1 V at a constant current density of 1 A/g; (b) discharge time for electrodes with varying fiber diameter, discharged from 1 V at a constant areal current of 20 μA/cm^2 of active surface area.

Discharge time exhibits a 1/D relationship with fiber diameter (Fig. 6a) up to around 230 nm, after which discharge time again begins to increase. The change from decreasing t_d to increasing t_d results from a shift between the scaling effect-controlled regime below 230 nm to a porosity-controlled regime above 230 nm. Scaling the required current to active surface area, as calculated by s_v multiplied by the area and thickness, L, of the 15 mm electrodes removes the 1/D dependence in the low-diameter region and reveals the second dominant trend controlling discharge time (Fig. 6b). When areal current is used, the curve is proportional to the inverse of porosity, and as porosity approaches zero, a sharp increase in discharge time is observed. Electrode porosity controls solution conductivity within the electrode pores as described by Eq. (16), which becomes the dominant component of the system time constant, τ, at low porosity (Eq. 15). At high porosity, the $1/\sigma$ matrix conductivity term controls the time constant, but as porosity approaches zero the $1/\kappa_p$ porosity-controlled term inflates the time constant, leading to a longer discharge time. Physically, the effect is caused by decreasing electrolyte conductivity, which results in lower ion transport rates, slower charge transfer, and ultimately a slower electrode response.[40,55] The lower power density caused by long discharge times is not generally desirable, although the increased surface area associated with minimal porosity works to increase energy density. However, surface area can also be increased in the system by maintaining a small fiber diameter and decreasing the center-to-center fiber spacing. By increasing the number of fibers in a unit cell of the electrode, surface area for energy storage can be maximized while maintaining high porosity to prevent restricting the electrolyte conductivity.

Power and energy densities were calculated according to

$$Energy\ density = \frac{I_{cell}\phi_{avg}t_d}{V_{cell}} \quad (23)$$

$$Power\ density = \frac{I_{cell}\phi_{avg}}{V_{cell}} \quad (24)$$

where I_{cell} is the total cell current applied, calculated as the product of current density, cell volume, and active volume (1 - ϵ); t_d is discharge time; V_{cell} is the volume of the full cell, including electrolyte, separator, and both electrodes; and ϕ_{avg} is the average cell potential over the entire discharge period as defined by

$$\phi_{avg} = \frac{1}{t_d}\int_0^{t_d}\phi_{cell}dt \quad (25)$$

where ϕ_{cell} is the cell potential measured between the two electrodes. Ragone plots were generated to examine the effect of the unique electrode morphology on power and energy densities (Fig. 7).

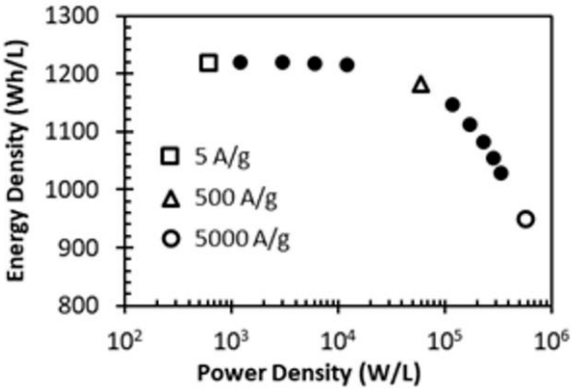

Figure 7: Ragone plot for electrospun electrode with fiber diameter, D = 115 nm. Current densities used to generate plot range from 5 A/g to 5000 A/g.

Ragone plots constructed for the modeled electrospun electrodes exhibit theoretical power and energy densities equal or superior to nanoparticle-based $RuO_2 \cdot xH_2O$ electrodes previously modeled.[25,34,56] While theoretical models are not readily available for electrospun carbon or oxide/carbon composite electrodes,

comparisons to real electrospun structures also demonstrates superior performance.[18,20] In the real system, a high-performance electrospun ZnO-carbon nanofiber electrode possesses an energy density of around 20 Wh/kg at power densities between 400 and 4000 W/kg. For Mn_2O_3 electrospun electrodes with average fiber diameter of 115 nm, the theoretical power density is approximately 270 Wh/kg at an energy density of 400 W/kg. Because carbon-based structures have lower theoretical capacitance than manganese oxides and real systems rarely perform near ideal, the difference between the performance of a real oxide-carbon composite electrode and an idealized, pure oxide electrode is reasonable.

In addition to high performance, the modeled electrodes exhibit remarkably stable energy densities over a wide range of power densities. Between 5 A/g and 500 A/g current densities, nearly no change in energy density is observed, dropping from 1219 Wh/L at 5 A/g to 1217 Wh/L at 500 A/g. Above 500 A/g the change in energy density becomes more apparent, but is still quite minor; at 5000 A/g the theoretical energy density of the electrospun electrodes remains at 952 Wh/L—only a 22 % decrease from maximum energy density with over a 93,000 % increase in power density. By comparison, similar changes in power density for nanoparticle-based RuO_2 structures are predicted to exhibit energy density drops of over two orders of magnitude. By altering current density, power density achieved by the cell can be increased by several orders of magnitude while maintaining energy densities within a single order of magnitude. The potential to improve the range of power densities available to power-dependent applications without a significant negative effect on the energy densities has exciting

prospects for implementing the structures in a wider range of applications with flexible power and energy requirements.

To examine model fidelity, predicted discharge curves were compared to actual curves collected with GCD from Mn_2O_3 electrospun electrodes (Fig. 8).

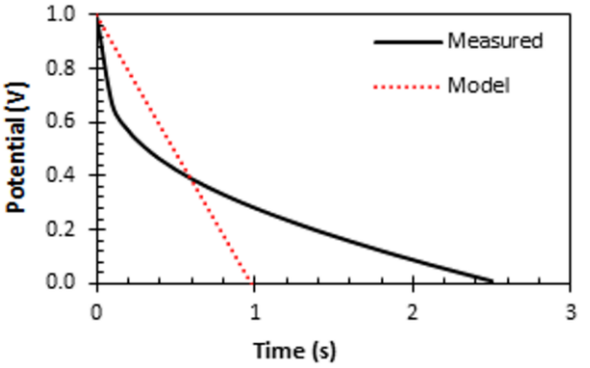

Figure 8: Discharge curve for modeled electrode with fiber diameter, D = 115 nm vs. measured discharge curve from real electrode with average fiber diameter of 112 nm. Electrodes were discharge from 1 V at a current density of 10 A/g. Color available online.

While the modeled discharge curve shows good correlation with other theoretical models,[34] it departs from actual discharge curves produced by performing GCD on the electrospun electrodes. The sharp initial drop observed in real electrodes is a true capacitive response to the current draw, where the faradaic reactions are too slow to provide the required current; the slope change that occurs after 1-2 s shows the region where pseudocapacitance and faradaic exchange become dominant in the system. The low slope of the discharge curve suggests that the faradaic response in the actual system is more dominant than predicted by the model. True capacitive response therefore accounts for a smaller amount of energy storage than anticipated, further supporting the

state of charge results presented in Figure 3, where it was determined that faradaic energy storage was essential to the system.

The discrepancy between the model and experimental results is explained by the characterization techniques used to measure faradaic and capacitive parameters; high-frequency EIS was used to measure DL capacitance of the system, while slow LSV was used to find exchange current density. Using two individual methods at different rates does not account for temporal effects in the system that may affect the balance between faradaic and capacitive response in the electrospun electrodes. The model does not account for the lag in faradaic response, nor the actual dominance of the faradaic response in the electrospun system. It is well-known that measured parameters such as DL capacitance can vary wildly with characterization technique (e.g., CV and GCD can give largely different capacitance values on the same sample), so the wide variety of techniques used to measure characteristic parameters of the electrospun system also worked to reduce model fidelity. However, further characterization of the Mn_2O_3 systems and electrodes composed of other oxides will serve to improve model accuracy by providing a more accurate estimate of system parameters.

V. SUMMARY AND CONCLUSIONS

A mathematical model with experimentally-derived parameters was produced to describe the performance of Mn_2O_3-based freestanding electrospun electrodes. A theoretical model based on capacitive and faradaic energy storage processes was used to examine the effects of fiber diameter and current density on discharge time, energy density, and power density. The unique effects of freestanding web electrode geometry

on performance were evident by way of their discharge behavior: with constant current density scaled to electrode mass, discharge time decreases with increasing fiber diameter up to 230 nm, then increases rapidly as porosity approaches zero. It is apparent that the optimized structure will combine small fiber diameters with a smaller interfiber spacing to maximize active surface area while maintaining high porosity. Comparison to real discharge curves shows that the model underestimates the capacitive response during initial discharge and the importance of the faradaic reactions over the remainder of the discharge period. A primary difficulty in producing an experimentally-based theoretical model is the necessity of mixing characterization techniques, but further characterization will improve model fidelity to result in greater accuracy and flexibility. The electrospun electrode structures exhibit remarkably high theoretical energy density retention with increasing power density, making them promising for applications with a wide range of power needs, including consumer electronics, load leveling, or transportation.

ACKNOWLEDGMENTS

Research was sponsored by the Combat Capabilities Development Command Army Research Laboratory and was accomplished under Cooperative Agreement Number W911NF-15-2-0020. The views and conclusions contained in this document are those of the authors and should not be interpreted as representing the official policies, either expressed or implied, of the Combat Capabilities Development Command Army Research Laboratory or the U.S. Government. The U.S. Government is authorized to reproduce and distribute reprints for Government purposes notwithstanding any copyright notation herein.

DATA AVAILABILITY

The data that support the findings of this study are available from the corresponding author upon reasonable request.

REFERENCES

[1] A.S. Aricò, P. Bruce, B. Scrosati, J.M. Tarascon, and W. Van Schalkwijk, Nat. Mater. **4**, 366 (2005).

[2] H.D. Yoo, E. Markevich, G. Salitra, D. Sharon, and D. Aurbach, Mater. Today **17**, 110 (2014).

[3] P. Simon and Y. Gogotsi, Nat. Mater. **7**, 845 (2008).

[4] M. Horn, J. MacLeod, M. Liu, J. Webb, and N. Motta, Econ. Anal. Policy **61**, 93 (2019).

[5] J.M. Boyea, R.E. Camacho, S.P. Turano, and W.J. Ready, Nanotechnol. Law Bus. **4**, 19 (2007).

[6] S. Banerjee, B. Di, P. Sinha, J. Cherusseri, and K.K. Kar, in *Handb. Nanocomposite Supercapacitor Mater. I. Springer Ser. Mater. Sci. Vol 300.*, edited by K.K. Kar (Springer, Cham., 2020), pp. 341–350.

[7] B.E. Conway, J. Electrochem. Soc. **138**, 1539 (1991).

[8] B.E. Conway, *Electrochemical Supercapacitors: Scientific Fundamentals and Technological Applications* (Springer Science and Business Media LLC, New York, 1999).

[9] G. Wang, L. Zhang, and J. Zhang, Chem. Soc. Rev. **41**, 797 (2012).

[10] P.J. Hall, M. Mirzaeian, S.I. Fletcher, F.B. Sillars, A.J.R. Rennie, G.O. Shitta-Bey, G. Wilson, A. Cruden, and R. Carter, Energy Environ. Sci. **3**, 1238 (2010).

[11] R. Kötz and M. Carlen, Electrochim. Acta **45**, 2483 (2000).

[12] D.B. Murray, J.G. Hayes, D.L. O'Sullivan, and M.G. Egan, IEEE J. Ocean. Eng. **37**, 301 (2012).

[13] A. González, E. Goikolea, J.A. Barrena, and R. Mysyk, Renew. Sustain. Energy Rev. **58**, 1189 (2016).

[14] A. V. Radhamani, M. Krishna Surendra, and M.S. Ramachandra Rao, Mater. Des. **139**, 162 (2018).

[15] C. Choi, D.S. Ashby, D.M. Butts, R.H. DeBlock, Q. Wei, J. Lau, and B. Dunn, Nat. Rev. Mater. **5**, 5 (2020).

[16] X. Lu, C. Wang, F. Favier, and N. Pinna, Adv. Energy Mater. **7**, 1601301 (2017).

[17] G. He, Y. Song, S. Chen, and L. Wang, J. Mater. Sci. **53**, 9721 (2018).

[18] Y. Cheng, L. Huang, X. Xiao, B. Yao, L. Yuan, T. Li, Z. Hu, B. Wang, J. Wan, and J. Zhou, Nano Energy **15**, 66 (2015).

[19] B. Vidhyadharan, N.K.M. Zain, I.I. Misnon, R.A. Aziz, J. Ismail, M.M. Yusoff, and R. Jose, J. Alloys Compd. **610**, 143 (2014).

[20] C.H. Kim and B.H. Kim, J. Power Sources **274**, 512 (2015).

[21] M. Brockway and J.L. Skinner, J. Vac. Sci. Technol. B Nanotechnol. Microelectron. **38**, 062401 (2020).

[22] W. Tiedemann and J. Newman, J. Electrochem. Soc. **10**, 849 (1965).

[23] V. Srinivasan and J.W. Weidner, J. Electrochem. Soc. **146**, 1650 (1999).

[24] B. Pillay and J. Newman, J. Electrochem. Soc. **143**, 1806 (1996).

[25] C. Lin, J.A. Ritter, B.N. Popov, and R.E. White, J. Electrochem. Soc. **146**, 3168 (1999).

[26] H. Kim and B.N. Popov, J. Electrochem. Soc. **150**, A1153 (2003).

[27] C. Lin, B.N. Popov, and H.J. Ploehn, J. Electrochem. Soc. **149**, A167 (2002).

[28] H.L. Girard, H. Wang, A.L. D'Entremont, and L. Pilon, Electrochim. Acta **182**, 639 (2015).

[29] C. Hao, X. Wang, Y. Yin, and Z. You, J. Electron. Mater. **45**, 515 (2016).

[30] J.A. Staser and J.W. Weidner, J. Electrochem. Soc. **161**, E3267 (2014).

[31] G. Sikha and B.N. Popov, Funct. Mater. Lett. **1**, 155 (2008).

[32] G. Sikha, R.E. White, and B.N. Popov, J. Electrochem. Soc. **152**, A1682 (2005).

[33] N. Aghamirzaie, V. Esfahanian, A. Jafari, and M.T. Dalakeh, J. Electrochem. Soc. **166**, A3660 (2019).

[34] H. Farsi and F. Gobal, J. Solid State Electrochem. **13**, 433 (2009).

[35] R.H. Nilson, M.T. Brumbach, and B.C. Bunker, J. Electrochem. Soc. **158**, A678 (2011).

[36] P. Guillemet, T. Brousse, O. Crosnier, Y. Dandeville, L. Athouel, and Y. Scudeller, Electrochim. Acta **67**, 41 (2012).

[37] B.-A. Mei, B. Li, J. Lin, L. Pilon, and H. Samueli, J. Electrochem. Soc. **164**, 3237 (2017).

[38] K. Dai, X. Wang, W. Lv, and Z. You, Key Eng. Mater. **645**, 513 (2015).

[39] A.G. Kashkooli, S. Farhad, V. Chabot, A. Yu, and Z. Chen, Appl. Energy **138**, 631 (2015).

[40] I.S. Ike, S.E. Iyuke, and E.E. Kalu, J. Energy Storage **35**, 102221 (2021).

[41] I.S. Ike, I. Sigalas, and S.E. Iyuke, Phys. Chem. Chem. Phys. **18**, 28626 (2016).

[42] H. Wang and L. Pilon, J. Phys. Chem. C **115**, 16711 (2011).

[43] T. Kadyk and M. Eikerling, J. Electrochem. Soc. **161**, A239 (2014).

[44] D. Dunn and J. Newman, J. Electrochem. Soc. **147**, 820 (2000).

[45] K. Somasundaram, E. Birgersson, and A.S. Mujumdar, J. Electrochem. Soc. **158**, A1220 (2011).

[46] M.W. Verbrugge and P. Liu, J. Electrochem. Soc. **152**, D79 (2005).

[47] A. Mundy and G.L. Plett, J. Energy Storage **7**, 167 (2016).

[48] R. Core Team, *R: A Language and Environment for Statistical Computing* (R Foundation for Statistical Computing, Vienna, Austria, 2021).

[49] K. Soetaert, T. Petzoldt, and R.W. Setzer, J. Stat. Softw. **33**, 1 (2010).

[50] P. Iamprasertkun, A. Krittayavathananon, A. Seubsai, N. Chanlek, P. Kidkhunthod, W. Sangthong, S. Maensiri, R. Yimnirun, S. Nilmoung, P. Pannopard, S. Ittisanronnachai, K. Kongpatpanich, J. Limtrakul, and M. Sawangphruk, Nat. Publ. Gr. **6**, 37560 (2016).

[51] R. Jow and J.P. Zheng, Electrochim. Acta **145**, 3250 (1998).

[52] S. Geller, Acta Crystallogr. Sect. B Struct. Crystallogr. Cryst. Chem. **27**, 821 (1971).

[53] F. Hong, B. Yue, N. Hirao, Z. Liu, and B. Chen, Sci. Rep. **7**, 44078 (2017).

[54] M.C. Brockway and J.L. Skinner, MRS Adv. **4**, 2383 (2019).

[55] B. Pal, S. Yang, S. Ramesh, V. Thangadurai, and R. Jose, Nanoscale Adv. **1**, 3807 (2019).

[56] H. Farsi and F. Gobal, J Solid State Electrochem **11**, 1085 (2007).

TABLES

Table I: List of model parameters used to describe discharge of freestanding electrospun electrodes. The model parameters include the measured values for the parameters that are manipulated during discharge modeling.

Parameter	Value	Source
Exchange current density, i_0	1.29×10^{-5} A	Measured (LSV)
Anodic transfer coefficient, α_a	0.664	Measured (LSV)
Cathodic transfer coefficient, α_c	0.336	Measured (LSV)
Equilibrium potential at anode, U_a	0.371θ V	Eq. (7)
Equilibrium potential at cathode, U_c	$0.371(\theta - 0.406)$ V	Eq (8)
Charge of a fully oxidized electrode, $Q_{f,ox}$	0.391 C at D = 112 nm	Eq. (10)
Charge of a fully reduced electrode, $Q_{f,red}$	0 C	Lin, et. al [25]
Specific surface area of electrode, s_v	2.22×10^5 cm^2/cm^3 at D = 112 nm	Eq. (17)
Lattice spacing at electrode surface, h	9.41×10^{-8} cm	Geller [52]
System time constant, τ	1.05×10^{-3} at D = 112 nm	Eq. (14)
Areal capacitance of electrode, C_d	1.51×10^{-6} F/cm^2	Measured (EIS)
Electrode thickness, L	4.08×10^{-5} cm at D = 112 nm	Measured (SEM)
Conductivity of electrode matrix, σ	1×10^{-5} S/cm	Hong, et. al [53]
Conductivity of bulk electrolyte, κ_0	0.0667 S/cm	Measured (EIS)
Electrolyte conductivity within pores, κ_p	0.051 S/cm at D = 112 nm	Eq. (15)
Fiber diameter, D	Between 100 and 250 nm	Assumed
Electrode porosity, ϵ	0.8371 at D = 112 nm	Measured (SEM)

FIGURE CAPTIONS

Figure 1: SEM micrographs of electrospun fiber mat electrodes (a) used to measure porosity by threshholding (b) and calculating ratio of black pixels to total pixels.

Figure 2: A typical Bode plot for electrospun Mn_2O_3 electrodes, with the equivalent circuit model overlaid onto data. A representation of the equivalent circuit model used to measure system parameters is also displayed. Color available online.

Figure 3: Voltage of Mn_2O_3 electrospun electrodes as a function of state of charge obtained by integrating the LSV curve, with the linear approximation displayed as a dotted line. Color available online.

Figure 4: Micrograph images of electrospun Mn_2O_3 fibers. (a) SEM showing fiber porosity and layered structure. (b) TEM showing interior porosity of electrospun oxide fibers.

Figure 5: Discharge curves generated from the mathematical model for freestanding web electrodes with fiber diameters of 100, 160, and 220 nm at a current density of 1 A/g. Color available online.

Figure 6: (a) Time to fully discharge for electrodes with varying diameter, discharged from 1 V at a constant current density of 1 A/g; (b) discharge time for electrodes with varying fiber diameter, discharged from 1 V at a constant areal current of 20 $\mu A/cm^2$ of active surface area.

Figure 7: Ragone plot for electrospun electrode with fiber diameter, D = 115 nm. Current densities used to generate plot range from 5 A/g to 5000 A/g.

Figure 8: Discharge curve for modeled electrode with fiber diameter, D = 115 nm vs. measured discharge curve from real electrode with average fiber diameter of 112 nm. Electrodes were discharge from 1 V at a current density of 10 A/g. Color available online.

Journal of Vacuum Science Technology B

PLEASE CITE THIS ARTICLE AS DOI: 10.1116/6.0001276

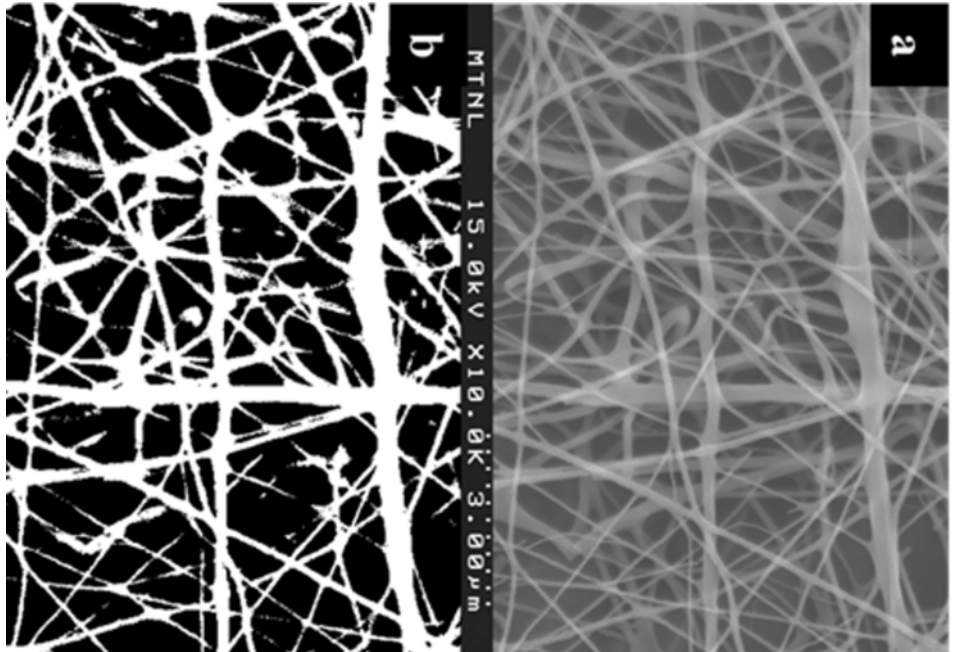

Journal of Vacuum Science Technology B

PLEASE CITE THIS ARTICLE AS DOI: 10.1116/6.0001276

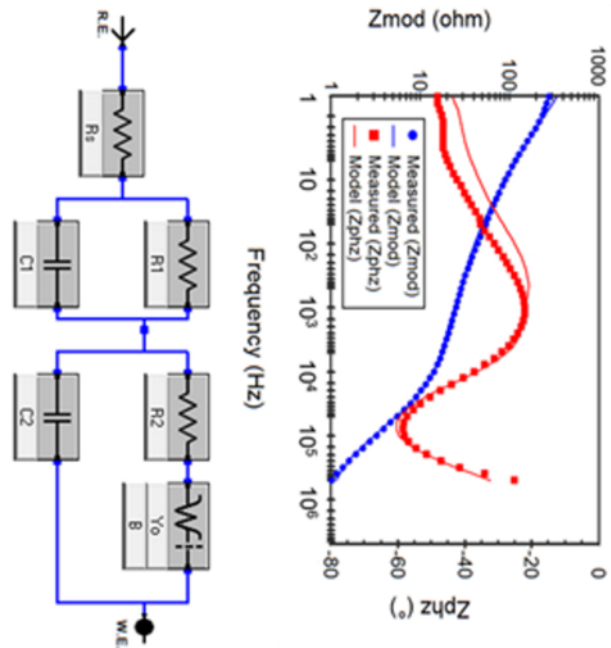

Journal of Vacuum Science Technology B

PLEASE CITE THIS ARTICLE AS DOI: 10.1116/6.0001276

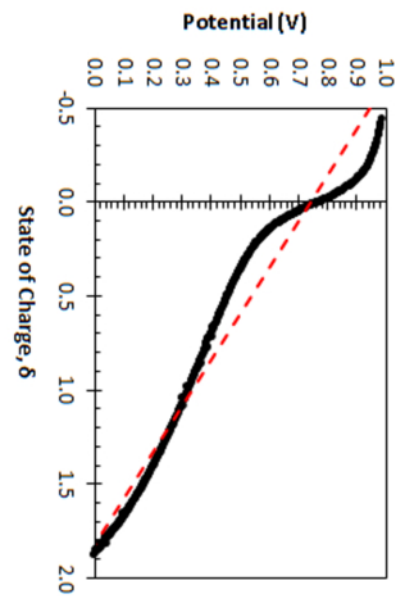

Journal of Vacuum Science Technology B

PLEASE CITE THIS ARTICLE AS DOI: 10.1116/6.0001276

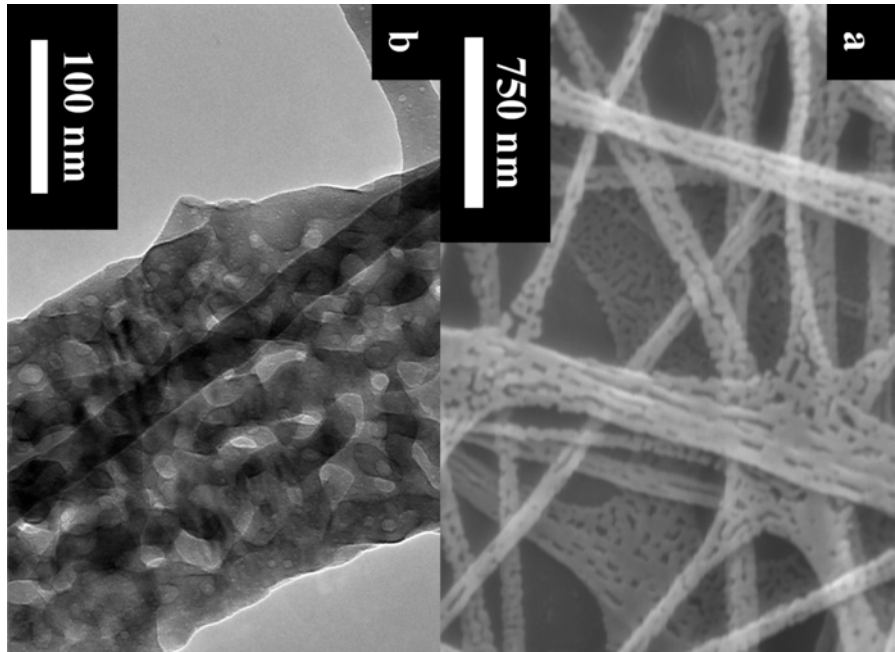

Journal of Vacuum Science Technology B

PLEASE CITE THIS ARTICLE AS DOI: 10.1116/6.0001276

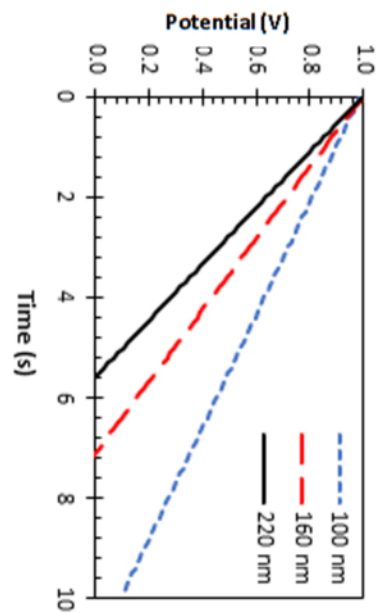

Journal of Vacuum Science Technology B

PLEASE CITE THIS ARTICLE AS DOI: 10.1116/6.0001276

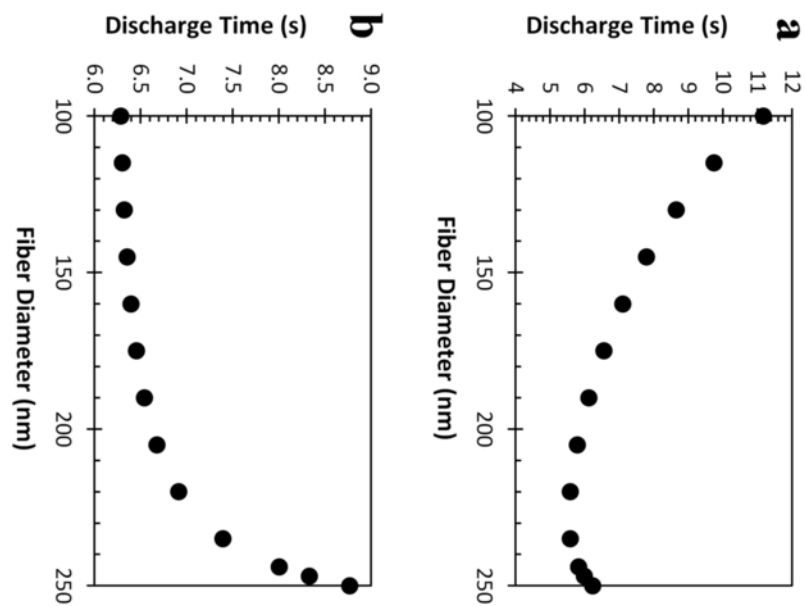

Journal of Vacuum Science Technology B

PLEASE CITE THIS ARTICLE AS DOI: 10.1116/6.0001276

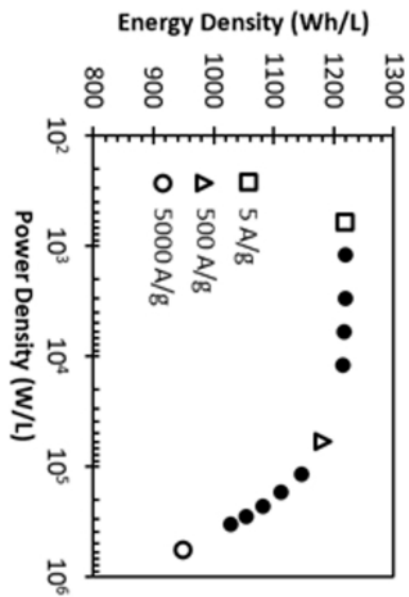

Journal of Vacuum Science Technology B

PLEASE CITE THIS ARTICLE AS DOI: 10.1116/6.0001276